Electronic correlation driven magnetic interactions in $Fe_{1-y}Co_ySn$ kagome semimetal

Kritika Vijay,[1,2] Kawsar Ali,[3] Kranti Kumar,[4] Archna Sagdeo,[1,2] Ashok Arya,[3] and Soma Banik[1,2,*]

[1]*Accelerator Physics and Synchrotrons Utilization Division, Raja Ramanna Centre for Advanced Technology, Indore 452013, India*

[2]*Homi Bhabha National Institute, Training School Complex, Anushakti Nagar, Mumbai 400094, India*

[3]*Glass and Advanced Materials Division, Bhabha Atomic Research Centre, Mumbai 400085, India*

[4]*UGC-DAE Consortium for Scientific Research, University Campus, Khandwa Road, Indore 452001, India*

(Received 19 January 2024; revised 28 May 2024; accepted 6 August 2024; published 30 August 2024)

Band engineering in magnetic kagome material has gained interest due to the emergence of novel quantum magnetism that arises from the interplay between topology and electron correlations. Here, we report a detailed study on the crystal structure, magnetization, and electronic structure of $Fe_{1-y}Co_ySn$ as a function of composition (y). The kagome lattice of $Fe_{1-y}Co_ySn$ is found to shrink with the increase in y. A decrease in the antiferromagnetic transition temperature (T_N) and changes in spin orientation is observed in the magnetization for $y > 0$. Core-level analysis showed a systematic decrease in the local moment of Fe and an increase in the local moment of Co with increasing y. Valence-band broadening and shifting of the bands away from the Fermi level (E_F) in Co-doped compositions are associated with enhanced hybridization and the correlation effects that give rise to localized and quasilocalized states near E_F. The band structure of FeSn (001) and $Fe_{0.95}Co_{0.05}Sn$ (001) surfaces along the $\bar{K}$-$\bar{\Gamma}$-$\bar{M}$ direction showed evidence of quasilocalized and localized flat bands. We find that there is an interplay between the Coulomb correlation and hybridization in Co-doped composition that gives rise to the broadening of the flat band and a shift of the Dirac point away from E_F and in k-space. The decrease in T_N with increasing y is associated with the correlation effects, which broaden the flat band and shift the Dirac point away from E_F, while the shift of the Dirac point in k-space is a signature of change in the magnetocrystalline anisotropy due to spin orientation.

DOI: 10.1103/PhysRevB.110.085163

I. INTRODUCTION

Kagome magnets have attracted immense interest due to the existence of exotic quantum states, which include the Dirac fermion, flat band, Weyl fermions, and van Hove singularity in its electronic structure [1–4]. These quantum states arise from unusual geometry in the kagome lattice and quantum interactions that lead to novel magnetism such as a quantum spin liquid [5,6], frustrated ferromagnetic (FM) and antiferromagnetic (AFM) ordering [7,8], chiral spin structures [9], etc. In recent years there has been a flurry of activity in engineering the flat bands with chemical pressure by doping in these kagome materials. Flat bands combine strong electron correlation and topological behavior, which means that their electronic structure cannot be deformed without changing the fundamental nature of the material. The flat band can be engineered in two ways with doping: (1) by bringing it closer to the E_F, which gives rise to exotic behavior and unusual phases, and (2) by increasing the density of localized flat band states near E_F, which means that there are many electrons with a similar energy, zero velocity, and an infinitely large effective mass. These factors have the effect of enhancing correlations between the electrons, which can lead to technologically important states, such as two-dimensional (2D) magnetism [10–12], superconductivity [13–15], etc.

In this article, we aim to study the band engineering in FeSn kagome magnet with Co doping. FeSn has a 2D kagome lattice with a 3D crystal structure [16]. The magnetic unit cell of FeSn is double the chemical unit cell along the c-axis [17]. In FeSn, the AFM transition temperature T_N is reported to be 365 K [1,18], with the spin orientations in the [210] direction in the temperature range between 70 to 365 K [18]. Below 70 K, a spin-flip effect is reported in FeSn where the spin orientation changes to the [100] direction [18]. Co-doping in $Fe_{1-y}Co_ySn$ reduces the T_N from 365 to 0 K between $y = 0$ and 0.6, which has been attributed to the suppression of the net magnetic moments [19,20]. For $y > 0.6$, spin-glass-type behavior is reported [21,22]. The spin orientation within the kagome layers was also found to change from perpendicular to parallel along the c-axis with the increase in y [20]. Thus, the orientation of spins in this system can be controlled with the doping concentration as well as with the temperature [19].

Co-doping in FeSn behaves like electron doping as the Co atom has one electron more than the Fe atom in its electronic configuration [23]. Below T_N, the Sn atoms are reported to contribute to the indirect magnetic superexchange interactions between Fe atoms in the adjacent kagome layers, which give rise to the complex magnetism [24]. A decrease in the density of states (DOS) near the E_F is reported in $Fe_{1-y}Co_ySn$ with increasing y [21]. From angle-resolved photoelectron spectroscopy (ARPES) measurements, the position of the flat band and the Dirac point is observed below E_F at 0.23 and 0.3 eV, respectively, for FeSn [1]. From neutron diffraction studies, it

*Contact author: soma@rrcat.gov.in

has been predicted that Dirac nodes in FeSn are gapped with the Co doping due to the spin rotation [20]. Lee *et al.* claimed that there are pseudospins involved in the electron tunneling between kagome layers in FeSn [25]. Thus, the change in the spin orientation with the Co doping must be associated with the microscopic changes in the electronic structure that need to be explored in detail in $Fe_{1-y}Co_ySn$.

In general, the kagome lattice features flat bands that usually lead to electronic correlation effects. However, it has rarely been explored how electronic correlation, in turn, stabilizes a perfect kagome lattice in $Fe_{1-y}Co_ySn$. There are several reports on the magnetic [20,26,27] and electronic [1,19,28] properties of $Fe_{1-y}Co_ySn$, but there are still some questions that remain unanswered: (1) What are the changes in the flat band with Co doping in $Fe_{1-y}Co_ySn$? (2) How can the change in magnetic anisotropy due to Co doping in $Fe_{1-y}Co_ySn$ be visualized in electronic structure studies? (3) What causes the decrease of T_N with Co doping in $Fe_{1-y}Co_ySn$ and the kind of exchange interactions present? In the present work, we have answered all of these questions and explained the behavior of Fe and Co atoms for the unusual magnetism and topological properties in the Co-doped $Fe_{1-y}Co_ySn$ compositions having AFM ordering up to $y \approx 0.4$. We find that the lack of detailed electronic structure studies on the higher Co-doped FeSn single crystals may be due to the issue of obtaining conveniently bigger-sized single crystals. The higher Co doping in FeSn results in hexagonal needle-shaped crystals [19], and it is a real challenge to perform photoemission studies on the top of the needle. So, the electronic band structure has been presented up to $y \leqslant 0.17$ composition [19] in the literature. Hence, in this work, we have presented detailed experimental studies on both the polycrystalline samples with $y = 0$, 0.15, and 0.4 and single-crystal samples with $y = 0$ and 0.05. The lattice parameters were found to reduce with Co doping in FeSn leading to the interplay between interlayer and intralayer interactions in the kagome lattice, and complex magnetism. We find that there are two different types of flat bands with localized and quasilocalized characters associated with the intralayer and interlayer interactions, respectively. In FeSn, quasilocalized states were found to dominate over localized states, while with the Co doping the localization effect was found to increase. The detailed phenomena involved in the band engineering in $Fe_{1-y}Co_ySn$ and the mechanism for the decrease in T_N and spin orientation with Co doping due to the changes in the electronic structure have been explained.

II. EXPERIMENTAL AND THEORETICAL METHODS

Polycrystalline ingots of $Fe_{1-y}Co_ySn$ were prepared by arc-melting the constituent elements of 99.999% purity under an argon atmosphere. The ingots were subsequently annealed at 750 °C for 168 h in sealed quartz ampules with 5×10^{-6} mbar vacuum. The bulk compositions of the ingots were determined by a commercial scanning electron microscope (Philips, XL30CP) equipped with an energy-dispersive spectrometer (EDS) from Bruker (XFlashr Silicon Drift Detector). The actual compositions determined from EDS are $Fe_{0.97}Sn_{1.03}$, $Fe_{0.85}Co_{0.14}Sn_{1.01}$, and $Fe_{0.58}Co_{0.44}Sn_{0.98}$ and they are referred to as $y = 0$, 0.15, and 0.4, respectively. Single crystals of $Fe_{1-y}Co_ySn$ with $y = 0$ and 0.05 were grown via the flux method, i.e., slow cooling a melt with tin flux using a procedure similar to that mentioned in Refs. [20,23,26]. The final composition has been determined by EDS. X-ray diffraction (XRD) measurements were carried out on a circular disk cut from an ingot for polycrystals and on bulk single-crystal pieces using a commercial x-ray diffractometer from Bruker, model D8 Advance, with a Cu $K\alpha$ source. Temperature-dependent magnetization $M(T)$ at 0.1, 1, and 5 T magnetic fields (H) was measured using a commercial SQUID magnetometer (MPMS XL, M/s. Quantum Design, USA) in a zero-field-cooled protocol. Field-dependent magnetization M versus H up to 8 T was performed in the paramagnetic (PM) phase (at 390 K) and the AFM phase (at 4 K). Photoemission measurements were performed at the Angle-Resolved Photoelectron Spectroscopy beamline (ARPES, BL-10), Indus-2 synchrotron using a SPECS Phoibos 150 electron analyzer. Synchrotron x-ray photoelectron spectroscopy (SR-XPS) measurements were carried out using photon energy ($h\nu$) = 1078 eV at BL-10 with 0.5 eV energy resolution, while the valence-band (VB) measurements were carried out using a monochromatic He-1 source from SPECS (UVS 300) with $h\nu = 21.2$ eV excitation energy and 20 meV energy resolution at 20 K. Prior to the photoemission measurement, the surface of the ingot was cleaned by mechanical scraping with a diamond file in the preparation chamber under a vacuum of 5×10^{-11} mbar. The surface cleanliness was confirmed by the absence of C 1s and O 1s peaks at 284 and 531 eV, respectively. To compare the photoemission data of all y, we have performed the measurements in the AFM phase at 20 K. The resonant photoemission (RPES) measurements were performed across Fe $2p_{3/2}$ to 3d resonance using $h\nu$ in the range between 705 and 712 eV with 0.3 eV energy resolution and across the Co $2p_{3/2}$ to 3d resonance $h\nu$ between 775 and 783 eV with 0.33 eV energy resolution. High-resolution ARPES measurements were carried out at 20 K using $h\nu =$ 56 eV with 30 meV energy resolution and 0.1 deg angular resolution. The single crystals of FeSn and $Fe_{0.95}Co_{0.05}Sn$ were cleaved *in situ* at 5×10^{-11} mbar to get an atomically clean surface. The base vacuum during the photoemission measurement was 7×10^{-11} mbar.

Noncollinear magnetic calculations using density functional theory (DFT) were performed for $y = 0$ and 0.4 compositions of $Fe_{1-y}Co_ySn$. Projector augmented wave method [29] -based potentials with parametrization of Perdew, Burke, and Ernzerhof [30] for exchange-correlation, as implemented in the Vienna Ab-initio Simulation Package (VASP) [31], were used. The valence electronic configurations of Fe, Co, and Sn atoms considered in the calculation were $3d^74s^1$, $3d^84s^1$, and $5s^25p^2$, respectively. Spin-orbit coupling was also incorporated in the calculations. To simulate the AFM order in a pristine FeSn system, 12 atoms, viz., $1 \times 1 \times 2$ supercells of FeSn unit cell, were used in the calculations, while a 60-atom-based ($1 \times 1 \times 10$ supercells of FeSn unit cell) special quasirandom structure (SQS), as generated by the Monte-Carlo method implemented in the ATAT package [32], was used for the $Fe_{0.6}Co_{0.4}Sn$ phase. The reciprocal space of FeSn and the $Fe_{0.6}Co_{0.4}Sn$ phase was sampled by a $9 \times 9 \times 5$ and $9 \times 9 \times 1$ k-point grid, respectively, which is generated under the Γ-centered Monkhorst-Pack scheme [33].

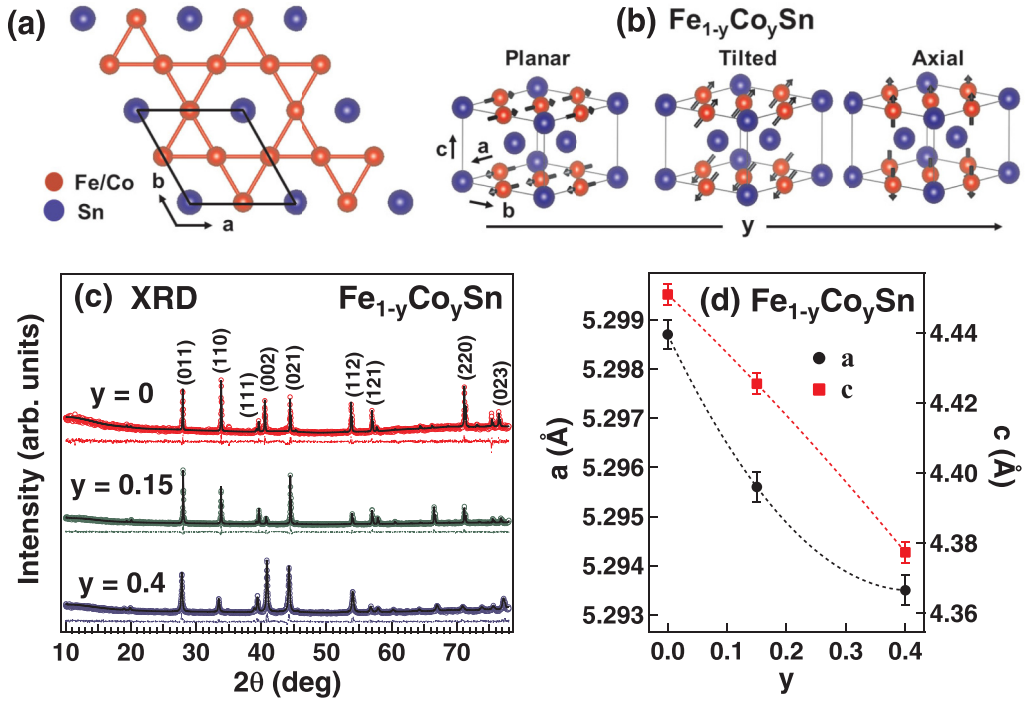

FIG. 1. (a) Arrangement of atoms in the kagome layer. (b) The magnetic structure of $Fe_{1-y}Co_ySn$ showing the spin orientation with an increase in y from planar to tilted and then to axial. The spins in the adjacent kagome layers are aligned antiferromagnetically in the $Fe_{1-y}Co_ySn$ system. (c) The XRD pattern of $Fe_{1-y}Co_ySn$ with $y = 0$, 0.15, and 0.4. The solid black line represents the calculated pattern using the Le Bail refinement, and the dashed lines represent the difference between the experimental and the calculated pattern in (c). (d) Lattice parameter variation as a function of composition y.

The cutoff energy of the plane waves was set to 500 eV in all the calculations.

III. RESULTS AND DISCUSSIONS

The kagome network of FeSn is shown in Fig. 1(a), which consists of corner-sharing triangles of Fe atoms and the hexagonal holes filled with Sn atoms [26]. In Fig. 1(b), the unit cell of FeSn with hexagonal B35 crystal structure [20] is shown, where Fe_3Sn layers are separated by Sn sheets [19,26]. The Fe spins are aligned ferromagnetically within the kagome layer and antiferromagnetically to the adjacent kagome layers along the c-axis [Fig. 1(b)] [20,26]. Co-doping in FeSn was reported to reorient the spins within the kagome layers [20]. The orientation of spins changes as a function of y in $Fe_{1-y}Co_ySn$ from planar to tilted and then to axial, as shown in Fig. 1(b) [19,20]. XRD patterns of all the compositions are shown in Fig. 1(c) confirming single-phase B35 hexagonal structure with space group $P6/mmm$ (No. 191). Lattice parameters a and c were determined by Le Bail refinement using the JANA2006 package [34]. Both a and c were found to decrease with an increase in y in $Fe_{1-y}Co_ySn$ [Fig. 1(d)], which agrees well with the reported results in Ref. [20]. The decrease in both a and c with the increase in y is associated with the atomic radius of Co (152 pm), which is smaller than that of Fe (156 pm) [22,35].

$M(T)$ for all y are shown in Figs. 2(a)–2(c) at different magnetic fields (H) = 0.1, 1, and 5 T. Vertical black dotted lines in Figs. 2(a), 2(b), and 2(c) denote the position of T_N at 365, 313, and 145 K for $y = 0$, 0.15, and 0.4, respectively. The slope change at low temperatures associated with the change in the magnetic interactions [18,22] is marked by an asterisk at 75, 70, and 55 K for $y = 0$, 0.15, and 0.4, respectively. The change in the shape of $M(T)$ curves is associated with the orientation of magnetic spins, which is reported to be planar for $y = 0$, tilted for $y = 0.15$, and axial for $y = 0.4$ in the ground state [20]. The dip at 155 K (marked by triangle) for $y = 0.15$ denotes the spin flip transition from tilted to axial [20,28]. The $M(T)$ curves presented here show a good matching with the results reported for single crystals in Ref. [20]. On comparing the $M(T)$ measured at 0.1, 1, and 5 T in Figs. 2(a)–2(c), we find that not only the value of M, but also the intensity of T_N increases with increasing H for all y. This phenomenon is associated with the magnetization controlled localization anisotropy [36]. Similar behavior of increasing $M(T)$ with an increase in H has been reported for spin glass materials [37,38] and noncollinear AFM systems [39]. In Figs. 2(d) and 2(e), $M(H)$ curves for all y at 390 K in the PM phase and at 4 K in the AFM phase are compared. We find strong FM correlations at low H below 1 T in FeSn ($y = 0$) in both PM and AFM phases, which could be due to the dominating FM interactions in the kagome layer. From neutron scattering studies it is reported that the spin waves in FeSn persisted well above T_N, suggesting that the in-plane FM spin correlations survive at high temperatures in Ref. [40], and the same has been observed in the $M(H)$ curve at 390 K in Fig. 2(d). It is also reported that there might be a second transition (a ferromagnetic-like transition) well above T_N as the in-plane FM coupling constant is much larger than the interplane AFM coupling [40]. Similar FM correlation above T_N has been reported in several layered AFM materials [41–43], which

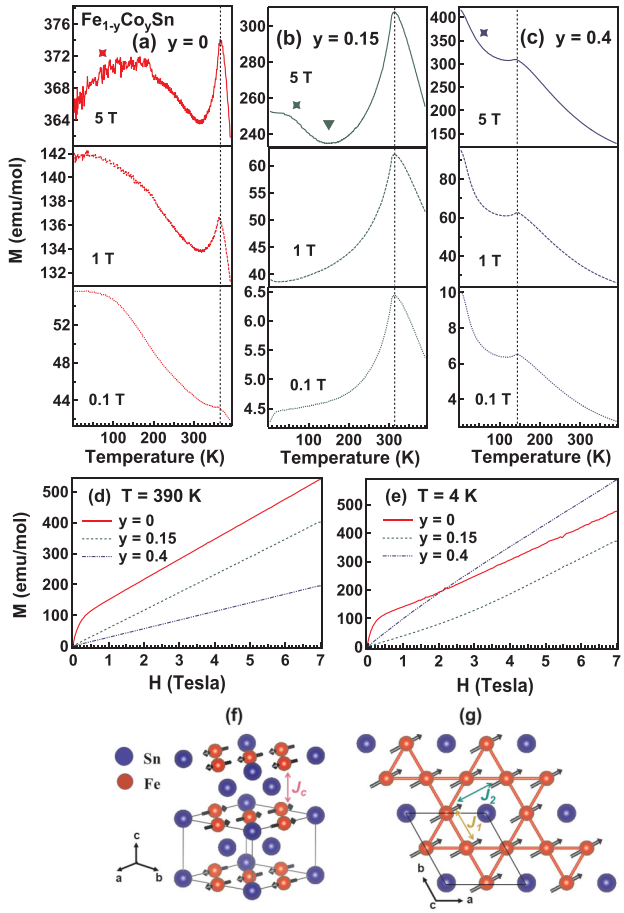

FIG. 2. $M(T)$ curves for (a) $y = 0$, (b) $y = 0.15$, and (c) $y = 0.4$ measured in the magnetic field (H) of 0.1, 1, and 5 T denoted by a dot-dashed, a dashed, and a solid line, respectively. T_N is marked by dashed lines in (a)–(c). $M(H)$ curves for all y in the PM phase at $T = 390$ K shown in (d) and in the AFM phase at $T = 4$ K shown in (e). Planar spin arrangement in FeSn showing the (f) out-of-plane (perpendicular direction to the kagome plane) and (g) in plane (along the kagome plane). J_1, J_2, and J_C are the exchange coupling between the atoms in-plane and out-of-plane as shown in (f) and (g).

indicates that the in-plane FM spin correlation is the intrinsic property in these types of materials. Deviation from linear $M(H)$ has also been reported in FeSn single crystal [26,27,44] along the easy axis of magnetization [kagome in-plane as shown in Fig. 2(g)]. We find that nonlinear behavior in $M(H)$ is much enhanced in the polycrystalline FeSn samples in the present study. The possible reason could be that in FeSn, Fe moments are localized in nature and collinear within the kagome layers with a planar orientation of spins [20,45,46] as shown in Figs. 2(f) and 2(g). The total exchange coupling J in FeSn has the contribution from J_1, which is in-plane nearest-neighbor exchange interaction; J_2, which is in-plane next-nearest-neighbor exchange interaction; and J_C, which is out-of-plane nearest-neighbor exchange interaction [45,46]. It is reported that the spin waves have FM in-plane dispersion and AFM out-of-plane dispersion with in-plane spin orientation along the easy axis [Fig. 2(g)] and out-of plane spin orientation along the hard axis [Fig. 2(f)] in Ref. [45]. The value of J_1 is reported to be much larger than J_2 and J_C in Refs. [45,46], which indicates that the dominating exchange interaction is the in-plane nearest-neighbor FM interaction. The magnetic phase diagram [20] showed planar spin orientation for FeSn in the whole temperature range from 365 K to 2 K, which indicates that the changes in the magnetization are associated with the change in the lattice parameter as a function of temperature. Hence, we can predict that in the PM phase the localized Fe moments in the adjacent kagome layers are well separated, but within the kagome layer there is short-range FM correlations due to the near-neighbor interactions J_1 and J_2, as shown in Fig. 2(g). It is reported that there is an anomalous suppression in the c-axis lattice constant when the temperature is decreased across the T_N, which increases the interaction between the adjacent kagome layers and hence gives rise to the AFM ordering [40]. Hence, there is an interplay between the FM and AFM correlations present in FeSn [40]. The reason for the enhanced nonlinear behavior of $M(H)$ in the polycrystalline FeSn sample compared with that in single crystals is because the grains are oriented in all the directions, and the contribution of the easy axis of magnetization, i.e., the kagome plane (in-plane) with the FM correlation, will be much higher than the hard axis of magnetization, i.e., perpendicular to the kagome plane (out-of-plane) with AFM correlations. Nearly linear $M(H)$ data were obtained for the Co-doped compositions $y = 0.15$ and 0.4, which shows good agreement with Ref. [27].

The XPS core levels of Fe, Co, and Sn in $Fe_{1-y}Co_ySn$ are shown in Fig. 3. The inelastic background has been subtracted from the raw data using the Tougaard method [47]. Solid lines in Fig. 3 are the fitting carried out using a least-squares error minimization routine with a Doniac-Sunjić-line shape [48]. The information about the exchange splitting and the local magnetic moment on Co and Fe atoms can be obtained from the Co 3s and Fe 3s core levels, as shown in Fig. 3(a). Fe 3s and Co 3s core-level data in Fig. 3(a) are a bit noisy due to the lower photoionization cross-section in XPS measurement. We have adopted the standard method for estimating exchange splitting and magnetic moment [49–51]. The exchange splitting (ΔE) of the Fe 3s peak is found to decrease from 4.9 to 4.3 eV between $y = 0$ and 0.4, while the exchange splitting of the Co 3s peak is found to increase from 3.3 to 3.6 eV between $y = 0.15$ and 0.4. Also the Fe 3s core level is found to shift towards lower binding energy (BE) as shown by ticks in Fig. 3(a), while the Co 3s core level is found to shift towards higher BE with the increase in y. The value of the local magnetic moment of Fe and Co atoms can be calculated from the intensity ratio of the majority peak to the minority peak of the 3s core levels [Fig. 3(a)], which is proportional to the relation $I = S/(S + 1)$, where S is the total spin [52]. Hence, the local magnetic moment can be calculated using the relation $M = g\sqrt{S(S+1)}\,\mu_B$, where g is the Landé g factor [51,52]. The estimated local magnetic moment per Fe atom is 2.83 μ_B, 2.66 μ_B, and 1.91 μ_B for $y = 0$, 0.15, and 0.4, respectively, while the local magnetic moment per Co atom is 1.62 μ_B and 1.65 μ_B for $y = 0.15$ and 0.4, respectively. The magnetic moments determined from the 3s core level in Fig. 3(a) are the static moment corresponding to the individual atoms. We find that with Co doping in $Fe_{1-y}Co_ySn$, the Fe local moment decreases, which causes a decrease in the value

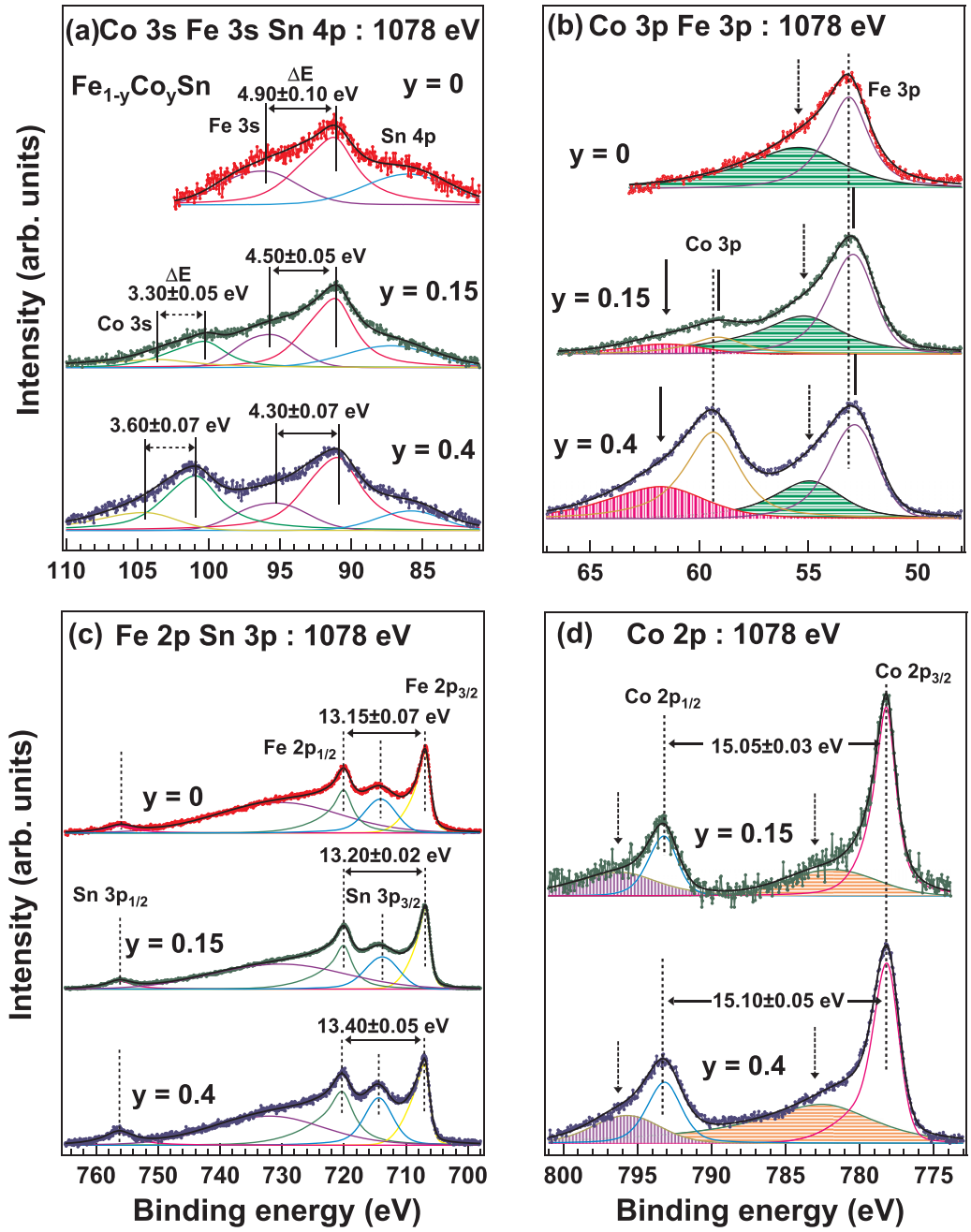

FIG. 3. XPS spectra of $Fe_{1-y}Co_ySn$ showing (a) Co 3*s*, Fe 3*s*, and Sn 4*p* core levels, (b) Co 3*p* and Fe 3*p* core levels, (c) Fe 2*p* and Sn 3*p* core levels for all the compositions, and (d) Co 2*p* core level for $y = 0.15$ and 0.4 compositions. The dotted and solid arrows in (a) indicate the exchange splitting between Co 3*s* peaks and Fe 3*s* peaks, respectively. The vertical dotted lines in (b) indicates the Co 3*p* peak for $y = 0.4$ and the Fe 3*p* peak for $y = 0$. The Co 3*p* correlation satellite peak position is shown by a solid arrow, while the Fe 3*p* correlation satellite peak position is shown by a dotted arrow. The horizontal solid arrows in (c) and (d) indicate the spin-orbit splitting of Fe 2p and Co 2p core levels peaks. The vertical dotted arrow in (d) represents the position of Co 2*p* correlation satellite peak.

of T_N, while the increase in the Co local moment is associated with on-site interaction between the Fe and Co local moment that gives rise to the spin reorientation [19,20]. The Sn 4*p* peak in Fig. 3(a) is found to shift towards lower BE with increasing *y* similar to the Fe 3*s* peak, indicating that Sn states carry the spin polarization. A similar shift of the Fe 3*p* peak towards lower BE and Co 3*p* peaks towards high BE has been observed in Fig. 3(b). Correlation satellites in Fe 3*p* and Co 3*p* core levels are marked by an arrow in Fig. 3(b), which indicates the localized character of the valence states. The increase in the intensity and width of the Co 3*p* peak and the correlation satellite are found to increase with Co doping, while the opposite is observed in the Fe 3*p* peak and its correlation satellite, which are found to have decreased intensity and width. Figures 3(c) and 3(d) show the value of spin-orbit splitting (SOS) of the Fe 2*p* and Co 2*p* core level peaks in $Fe_{1-y}Co_ySn$, which is found to be larger than pure Fe metal (13 eV) and Co metal (15 eV) [53]. The increase in SOS is associated with the near-neighbor

interactions and the hybridization present in $Fe_{1-y}Co_ySn$ [54]. Furthermore, with the increasing y we find that not only the SOS of both Fe $2p$ [Fig. 3(c)] and Co $2p$ [Fig. 3(d)] peaks increases but also the width of the Co $2p$ [Fig. 3(d)] peaks increases, which is in line with the changes observed in the Co $3p$ satellite [Fig. 3(b)]. This phenomenon is associated with the increase in hybridization with increased doping.

Fe-Fe interaction in $y = 0$ gives rise to intralayer FM ordering in the kagome plane and interlayer AFM interactions in the adjacent kagome planes. This can be explained as Fe has four unpaired electrons in the valence shell with the local moment of 2.83 μ_B/Fe atoms in FeSn. The intralayer interaction in FeSn depends mostly on the orbital overlap and hopping, while the interlayer interactions depend on the indirect exchange interaction through the spin polarization of the Sn atoms. In FeSn the interlayer AFM interaction is found to be dominating over the intralayer FM interactions as the valence orbitals of Sn atoms are more hybridized, and they participate in indirect magnetic superexchange-type interactions [24]. In the case of Fe-Co interactions in the doped compositions, Co has three unpaired electrons in the valence shell with a local magnetic moment of Co $\approx$1.62 μ_B, which is less than the local magnetic moment of Fe $\approx$2.66 μ_B for $y = 0.15$. Doping Co in the Fe site causes the spin-pairing of the moments, which gives rise to the intralayer FM-type interaction in the kagome plane and the interlayer AFM-type interaction due to the indirect exchange interaction between the small magnetic moments in the adjacent kagome planes. Hence, there is a competition between FM-type intralayer and AFM-type interlayer interactions in the higher doped compositions.

The local moment on both Fe and Co atoms gives rise to the correlation effects and localized states in $Fe_{1-y}Co_ySn$. Electron correlation energy U is defined as the energy required to transfer an electron within the same band between two ions in a solid, which are initially in the same valence state. U can be derived experimentally from the position of the electronic states using two different methods: (1) using photoemission and inverse photoemission to determine the energy position of $3d^{n-1}$ and $3d^{n+1}$ states, respectively [55], and (2) using resonant photoemission to determine the energy position of $3d^{n-1}$ and $3d^{n-2}$ states [56]. We have used the second method to determine the value of U experimentally using the Fe $2p_{3/2}$ to $3d$ and Co $2p_{3/2}$ to $3d$ RPES of $Fe_{1-y}Co_ySn$ as shown in Figs. 4(a)–4(c) and in Figs. 4(e) and 4(f), respectively. At the resonance we have observed a strong enhancement of the intensity for both Fe $3d$ and Co $3d$ states due to the increase of the photoionization cross-section and marked by a solid line in Fig. 4. Above the resonance we can observe that the Fe $3d$ and Co $3d$ features shows a shift towards higher BE with the increase in $h\nu$. This kind of behavior is related to the LVV Auger feature, which corresponds to a $2p$ (L-shell) initial state core-hole getting filled by a valence electron, and the available energy is used to remove another valence electron, resulting in a two valence hole (VV) final state similar to the $3d^{n-2}$ state [56]. The two holes repel each other by the on-site Coulomb energy $U = \{E_{2p} - (h\nu - E_{LVV})\} - 2\epsilon_{3d}$, which is the energy difference between the LVV Auger energy $[E_{2p} - (h\nu - E_{LVV})]$ and the average energy of two uncorrelated holes ($2\epsilon_{3d}$). E_{2p} and ϵ_{3d} are the BEs of the $2p$ core level (in Fig. 3) and the $3d$ state (in Fig. 5), respectively. E_{LVV} is the BE of the LVV auger feature. Thus, the values of U estimated for both Fe $3d$ and Co $3d$ states are shown in Fig. 4(d). We find that the value of U for Fe $3d$ states systematically increases from 2.4 to 2.55 eV between $y = 0$ and 0.4 while the value of U for Co $3d$ states systematically decrease from 2.55 to 2.5 eV. An increase in U_{Fe} and a decrease in U_{Co} indicate an increase in the hybridization strength due to the increase in the d-d interaction with the increase in y.

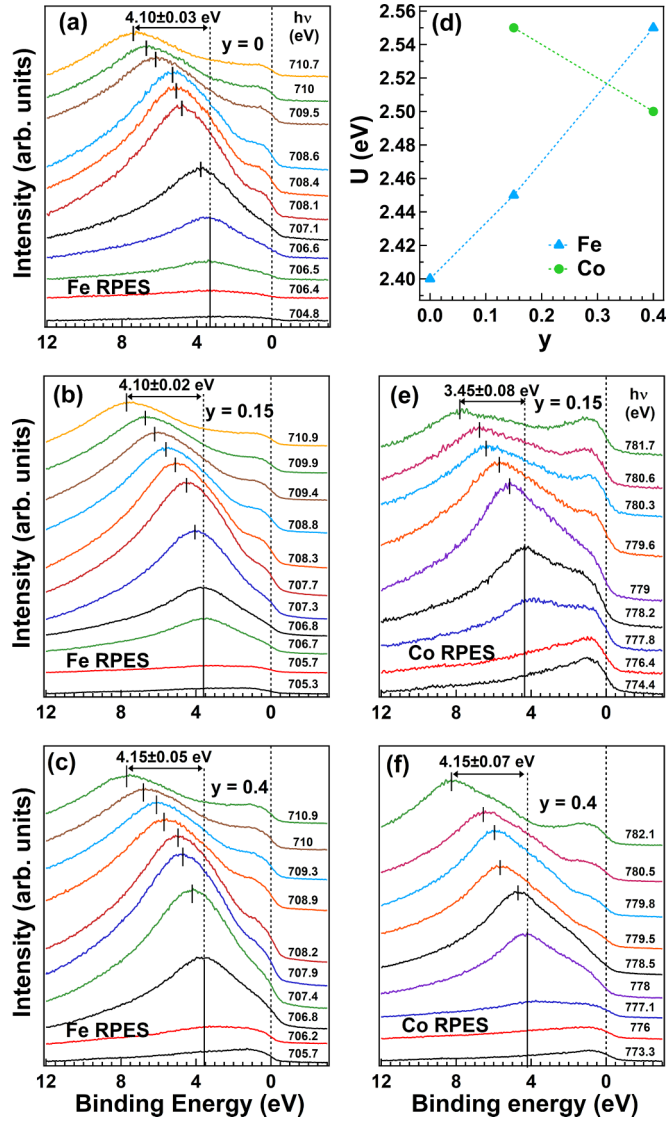

FIG. 4. RPES spectra recorded across Fe $2p_{3/2}$-$3d$ resonance for (a) $y = 0$, (b) $y = 0.15$, and (c) $y = 0.4$. RPES spectra recorded across Co $2p_{3/2}$-$3d$ resonance for (e) $y = 0.15$ and (f) $y = 0.4$. The estimated value of U as a function of y in $Fe_{1-y}Co_ySn$ for Co and Fe states is shown in (d).

High-resolution VB measurements on $Fe_{1-y}Co_ySn$ performed at RT (300 K) and LT (20 K) using 21.2 eV excitation energy are shown in Fig. 5(a). Seven prominent features marked as A, B, C, D, E, F, and G are observed in Fig. 5(a). These features were identified by comparing the VB features of elemental Co, Fe, and Sn metals with the measured spectra

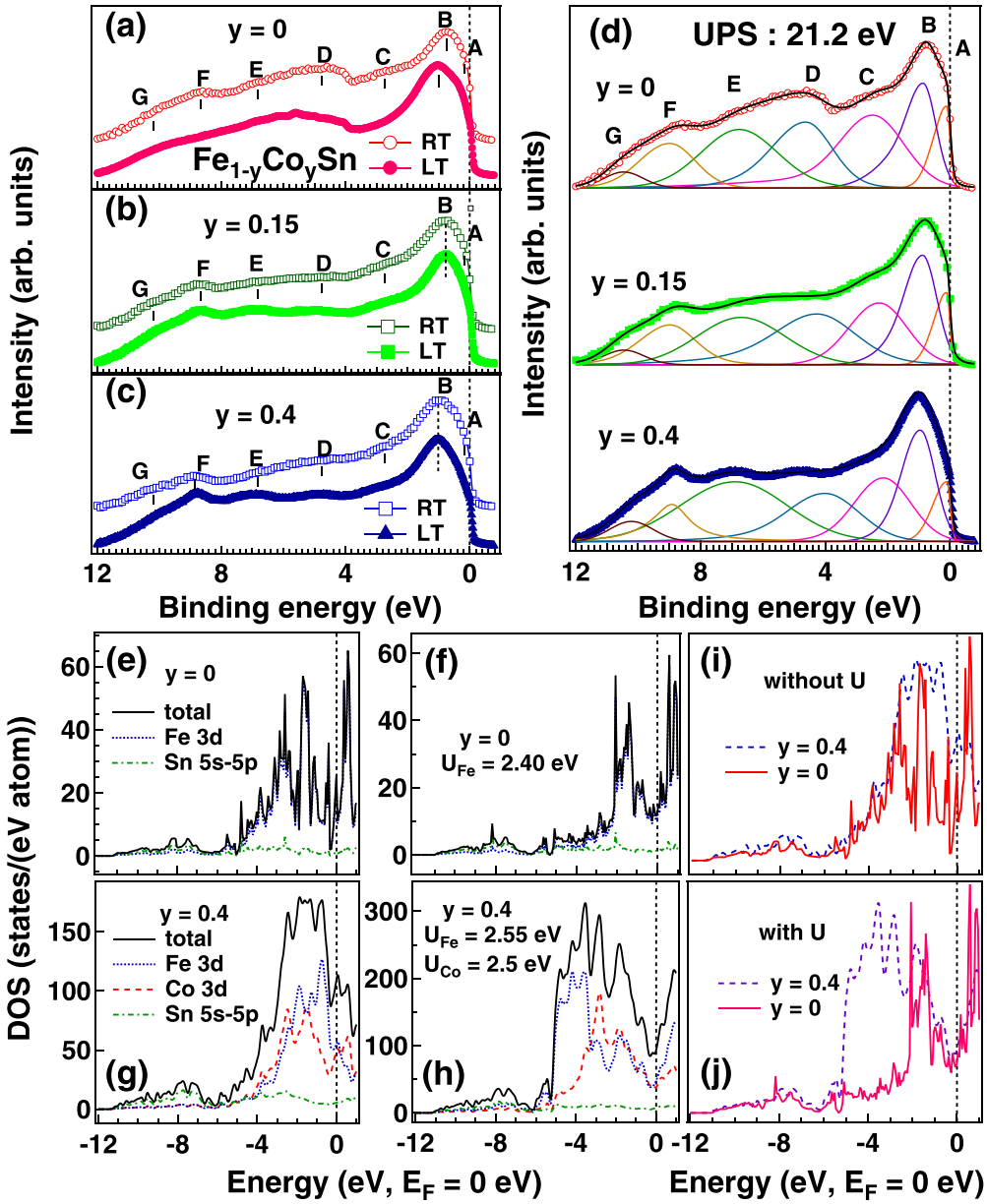

FIG. 5. The VB spectra of $Fe_{1-y}Co_ySn$ at RT (300 K) and LT (20 K) recorded using 21.2 eV photoexcitation energy for (a) $y = 0$, (b) $y = 0.15$, and (c) $y = 0.4$. (d) The wide VB spectra in the AFM phase of $y = 0$, 0.15 and 0.4 are fitted with Gaussian peaks, and the prominent states are indicated as A, B, C, D, E, F, and G. The theoretical GGA calculation showing total DOS, Fe 3*d* DOS, Co 3*d* DOS, and Sn 5*s*-5*p* DOS are shown for (e) $y = 0$ and (g) $y = 0.4$. The GGA + U calculations with U obtained from experimental results are shown in (f) $y = 0$ and (h) $y = 0.4$. The total normalized DOS for $U = 0$ and experimental U are compared in (i) and (j), respectively.

of $Fe_{1-y}Co_ySn$ alloys, and they are discussed in Ref. [22]. The feature A lies at 0.17 eV at both RT and LT for $y = 0$, near the flat band position reported in FeSn single crystal (∼0.23 eV) [1,19,22,45]. The position of the flat band is found to be at the same energy position for all y. Feature B is related to the Fe 3*d* bulk band at 0.85 eV for $y = 0$ at RT, which matches well with results reported in Ref. [19] (0.8 eV for $y = 0.06$). There is a shift in the feature B to 1 eV for $y = 0$ at LT which could be related to the complicated magnetic interactions at LT as observed in the $M(T)$ data in Fig. 2. Features C, D, and E are associated with hybridized Fe 3*d* and Sn 5*s*-5*p* states for $y = 0$. Features F and G correspond to Sn 5*s*-5*p* states for all compositions. In doped samples, feature B is associated with the bulk Fe 3*d* and Co 3*d* hybridized states. Features C, D, and E are related to hybridized Fe 3*d*, Sn 5*s*-5*p*, and Co 3*d* states. For the Co-doped compositions in Figs. 5(b) and 5(c), the VB features almost match at RT and LT. On comparing the VB spectra of $y = 0.15$ and 0.4 in Fig. 5(b) and 5(c), respectively, we find that feature B is shifted towards higher BE with the increase in doping concentration (see the vertical dashed line). $y = 0$ has AFM phase at both RT and LT with complicated magnetic interactions at LT. Hence, the fitting of VB spectra in the AFM phase performed at LT for $y = 0.15$ and 0.4 and RT for $y = 0$ using the Gaussian peaks as shown in Fig. 5(d). On comparing the intensity of features A and B, we find that the intensity of feature B increases while that of

feature A decreases with an increase in y. The bandwidth of both features A and B is found to increase with increasing y due to the increased hybridization between Co $3d$ and Fe $3d$ states. Feature B shifts 0.2 eV towards higher BE from E_F between $y = 0$ and 0.4, which is in line with the shifts observed in the Co $3s$ and Co $3p$ core-level peaks [in Figs. 3(a) and 3(b)]. Feature C shifts 0.38 eV towards lower BE between $y = 0$ and 0.4 [22], similar to Fe $3s$ and Fe $3p$ core levels [in Figs. 3(a) and 3(b)]. Features D and E are also found to be shifted towards lower BE with increases in y due to increased hybridization between Fe $3d$ and Sn $5s$-$5p$ states. Features F and G remain in the same position for all compositions corresponding to Sn $5s$-$5p$ hybridized states.

To understand the correlation between magnetic phases and the electronic structure, we have carried out noncollinear AFM generalized gradient approximation (GGA) calculations for $y = 0$ and 0.4 as shown in Figs. 5(e) and 5(g), respectively. We have also carried out GGA + U calculations for $y = 0$ and 0.4 in the AFM phase shown in Figs. 5(f) and 5(h), respectively, to explain the correlation effects observed in XPS and RPES results (Figs. 3 and 4). The U determined from experiment as discussed in Fig. 4 has been considered in the GGA + U calculations for $y = 0$ and 0.4 in Figs. 5(f) and 5(h). For comparing the calculations with the experimental results, we have shown the total DOS by adding partial DOSs after multiplying with the photoionization cross-section at 21.2 eV excitation energy. The total DOS with $U = 0$ and experimental values of U have been compared for $y = 0$ and 0.4 compositions in Figs. 5(i) and 5(j). Considering $U = 0$ eV in the GGA calculation [Fig. 5(i)] for $y = 0$ and 0.4 we find two prominent differences with the experiment: (1) there are sharp DOSs near E_F for $y = 0$ which are further enhanced for $y = 0.4$, and (2) The $3d$ states of $y = 0$ and 0.4 are found to be at similar energy positions in Fig. 5(i) with no signature of valence-band broadening. Hence, the calculated VB with $U = 0$ eV [Fig. 5(i)] does not show good agreement with the experimental VB [Figs. 5(a) and 5(c)]. Further considering the contribution of U in the GGA + U calculations as shown in Fig. 5(j), we find that the sharp peaks in the DOS near E_F are broadened and show a depletion of states near E_F for both $y = 0$ and 0.4, which is typical of semimetallic character. Moreover, there is also shift of the $3d$ states away from E_F for $y = 0.4$ as compared to $y = 0$. A similar trend of shifting of feature B towards higher BE has been observed in the experiment [Figs. 5(a)–5(d)] with increasing y. The VB width for $y = 0.4$ in the calculation is found to be much broader than $y = 0$ in Fig. 5(j), which agrees well with the experimental VB. The broadening of the VB is associated with the increase in hybridization due to the orbital overlap with doping. Hence, the interplay of hybridization and on-site U on Co and Fe atoms drives the complex magnetism in this system.

To better understand the flat band and Dirac point in this system, we have performed the ARPES measurements on $y = 0$ and 0.05 compositions on the (001) surface using $h\nu = 56$ eV along the $\bar{K}$-$\bar{\Gamma}$-$\bar{M}$ direction at 20 K (AFM phase). We can clearly see that in FeSn there is a faint flat band [marked as FB in Fig. 6(a)] near E_F around 0.16 eV and a Dirac point [marked as DP in Fig. 6(a)] at 0.3 eV. A similar position of DP and FB in FeSn was reported in Ref. [28]. In the case of

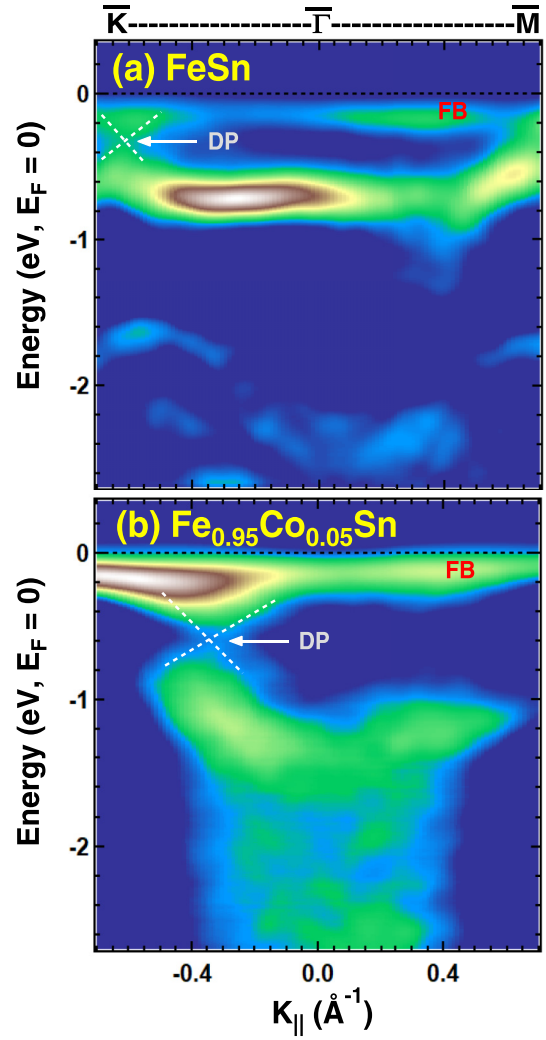

FIG. 6. Band mapping of (a) FeSn (001) and (b) $Fe_{0.95}Co_{0.05}Sn$ (001) surface in the AFM phase (20 K).

$y = 0.05$ ($Fe_{0.95}Co_{0.05}Sn$), we can see that the FB near the E_F becomes quite intense, and moreover there is a shift of the DP away from E_F to about 0.6 eV. A similar shift of the DP with Co doping in FeSn is also reported in Ref. [19]. Hence, the quasilocalized behavior gives rise to the faint kagome FB near E_F in FeSn, while the increase in the localization effect is observed in the Co-doped FeSn sample, which increases the density of FB states. A similar broadening of the states near E_F [see feature A in Fig. 5(d)] and a shifting of the states near E_F [see feature B in Fig. 5(d)] have also been observed in the polycrystalline samples. The broadening of the FB and the shifting of the DP is due to the interaction between the Fe and Co $3d$ electrons in the Co-doped composition ($y = 0.05$). The DP at 0.6 eV as observed in $y = 0.05$ [Fig. 6(b)] is also reported in CoSn [57], which confirms that the Co is doping at the Fe site in the kagome lattice, and electron correlation increases with Co doping.

Flat bands provide a roadmap for bridging topology with correlation in these kagome materials. In this work, we have seen that there is a reduction in the T_N with the Co doping in FeSn in the magnetization studies. Also spin canting is reported from neutron diffraction in Ref. [20] for the Co-doped

FeSn alloys. On comparing the photoemission studies with the magnetization, we can see that the quasilocalized FB in FeSn gives rise to higher values of T_N while the broader FB with more localized character in $y = 0.05$ [Fig. 6(b)] gives rise to lower values of T_N. Moreover, spin canting, which is associated with the change in the magnetocrystalline anisotropy, has a prominent signature in the ARPES data, where we find that there is a shift in the DP in k-space near the Γ-point with the Co doping in FeSn. For $y = 0$ the DP is observed at $K_{||} = 0.65$ Å^{-1}, while for $y = 0.05$ it is observed at $K_{||} = 0.35$ Å^{-1}. This is a clear indication of the change in the magnetocrystalline anisotropy due to the change in the spin orientation. A similar observation of shifting of the bands in the k-space due to the change in the magnetocrystalline anisotropy has been reported by us for PrGe in Ref. [58].

Thus, the macroscopic mechanism for complex magnetism in $Fe_{1-y}Co_ySn$ with Co doping is associated with localized-quasilocalized phenomena, as also observed in CoSn [22]. This phenomena is also seen in the rare-earth systems, which have very localized $4f$ states, and the valence electrons that participate in conduction can have both localized and delocalized character of $4f$ electrons with the system having metallic bonding [55,59,60]. In such systems, hybridization between the localized band with the conduction band in an atom plays a role in the observation of exotic electronic states. In the present case, a localized $3d$ flat band in FeSn due to its special geometry was found to have a similar behavior as the localized bands in rare-earth systems. We find that the localized $3d$ band of Fe in FeSn is hybridized with the Fe $4s$ and Sn $5s$-$5p$ conduction electrons and hence the $3d$ bands also have itinerant character. With the Co doping at the Fe site in the kagome lattice, we find that both the Co and Fe $3d$ states are hybridized, and there is an increase in the localization effect. The extra $3d$ electrons of Co increase the localization effect and are responsible for the complex magnetism. The signature of quasilocalized and localized states also observed in the features A and B in the VB spectra [Fig. 5(d)]. In FeSn the localized states arise due to the intralayer interaction between Fe-Fe atoms in the kagome plane, while the quasilocalized states arise due to the hybridization between the Fe-Sn atoms, which gives rise to the interlayer indirect exchange interaction in the adjacent kagome planes. The contribution of quasilocalized states dominates over localized states in FeSn, which gives rise to the AFM ordering. With the Co doping in FeSn, the contribution of the localized states increases over the quasilocalized states. An increase in Fe localized states increases the value of U_{Fe}, while Co states are hybridized with the Fe and Sn states, which showed a decrease in the value of U_{Co} with an increase in y. The interplay of hybridization and on-site U causes the decrease in the quasilocalized DOS near E_F, which causes the decrease in the local magnetic moment of Fe and the value of T_N with increasing y. The increase in the spin-orbit coupling [Figs. 3(c) and 3(d)] with doping due to the strong spin pairing and hybridization between Fe and Co states causes the spin reorientation in this system.

IV. CONCLUSION

We find that with the Co-doping in FeSn, the kagome lattice gets stabilized by increasing the intralayer interaction and decreasing the interlayer interaction between the adjacent kagome layers. The increase in the intralayer interaction with Co doping increases the correlation effects and gives rise to a more localized flat band, while the decrease in the interlayer interaction between the adjacent kagome layers with Co-doping in $Fe_{1-y}Co_ySn$ gives rise to a decrease in T_N and spin canting in this system. This phenomenon is quite evident in the band-structure studies, where we have seen the shifting of the Dirac point away from E_F and towards the Γ point in k-space, and also in the core-level studies, where an increase in the spin-orbit splitting is observed for both Co and Fe atoms. A systematic decrease in the local magnetic moment of Fe atoms and an increase in the local moment of Co atoms is obtained with the increase in y. Moreover, the exchange interaction between the Fe atoms is found to decrease, while the exchange interaction between Co atoms is found to increase due to the influence of the electron correlation energy. We have observed a quasilocalized flat band in FeSn, while with the increase in Co-doping in $Fe_{1-y}Co_ySn$ the density of flat band states increases and becomes more localized. An increase in the density of flat band states in Co-doped $Fe_{1-y}Co_ySn$ alloy implies that there is an enhanced electron correlation effect, which has important technological applications in spintronics and thermoelectricity.

ACKNOWLEDGMENTS

The authors wish to thank S. V. Nakhe, Director, RRCAT, and Tapas Ganguli, Head, APSUD, for their constant encouragement and support. K.V. acknowledges the financial support for fellowship from Raja Ramanna Centre for Advanced Technology, Indore and Homi Bhabha National Institute, Mumbai. Ravindra Jangir is thanked for providing the high-temperature box furnace. Pragya Tiwari and Rashmi Singh are thanked for the energy dispersive spectroscopy measurements. S. K. Ramjan is thanked for his help in the preparation of polycrystalline samples using the arc-melting technique. Suvankar Paul is thanked for his help in the photoemission measurements. L. S. Sharath Chandra is thanked for scientific discussions and a thorough reading of the manuscript.

[1] M. Kang, L. Ye, S. Fang, J.-S. You, A. Levitan, M. Han, J. I. Facio, C. Jozwiak, A. Bostwick, E. Rotenberg, M. K. Chan, R. D. McDonald, D. Graf, K. Kaznatcheev, E. Vescovo, D. C. Bell, E. Kaxiras, J. v. d. Brink, M. Richter, M. P. Ghimire *et al.*, Nat. Mater. **19**, 163 (2020).

[2] J. X. Yin, B. Lian, and M. Z. Hasan, Nature (London) **612**, 647 (2022).

[3] Z. Ren, H. Li, S. Sharma, D. Bhattarai, H. Zhao, B. Rachmilowitz, F. Bahrami, F. Tafti, S. Fang, M. P. Ghimire, Z. Wang, and I. Zeljkovic, npj Quantum Mater. **7**, 109 (2022).

[4] Y. Hu, X. Wu, B. R. Ortiz, S. Ju, X. Han, J. Ma, N. C. Plumb, M. Radovic, R. Thomale, S. D. Wilson, A. P. Schnyder, and M. Shi, Nat. Commun. **13**, 2220 (2022).

[5] L. Balents, Nature (London) **464**, 199 (2010).

[6] C. Broholm, R. J. Cava, S. A. Kivelson, D. G. Nocera, M. R. Norman, and T. Senthil, Science **367**, eaay0668 (2020).

[7] Y. Taguchi, Y. Oohara, H. Yoshizawa, N. Nagaosa, and Y. Tokura, Science **291**, 2573 (2001).

[8] S. Nakatsuji, N. Kiyohara, and T. Higo, Nature (London) **527**, 212 (2015).

[9] M. Pereiro, D. Yudin, J. Chico, C. Etz, O. Eriksson, and A. Bergman, Nat. Commun. **5**, 4815 (2014).

[10] H. Huang, L. Zheng, Z. Lin, X. Guo, S. Wang, S. Zhang, C. Zhang, Z. Sun, Z. Wang, H. Weng, L. Li, T. Wu, X. Chen, and C. Zeng, Phys. Rev. Lett. **128**, 096601 (2022).

[11] J.-X. Yin, S. S. Zhang, G. Chang, Q. Wang, S. S. Tsirkin, Z. Guguchia, B. Lian, H. Zhou, K. Jiang, I. Belopolski, N. Shumiya, D. Multer, M. Litskevich, T. A. Cochran, H. Lin, Z. Wang, T. Neupert, S. Jia, H. Lei, and M. Zahid Hasan, Nat. Phys. **15**, 443 (2019).

[12] G. Bouzerar, Phys. Rev. B **107**, 184441 (2023).

[13] H. Aoki, J. Supercond. Novel Magn. **33**, 2341 (2020).

[14] M. Thumin and G. Bouzerar, Phys. Rev. B **107**, 214508 (2023).

[15] R. Khasanov, B.-B. Ruan, Y.-Q. Shi, G.-Fu Chen, H. Luetkens, Z.-A. Ren, and Z. Guguchia, Nat. Commun. **15**, 2197 (2024).

[16] N. J. Ghimire and I. I. Mazin, Nat. Mater. **19**, 137 (2020).

[17] K. Yamaguchi and H. Watanabe, J. Phys. Soc. Jpn. **22**, 1210 (1967).

[18] S. Ligenza, Phys. Status Solidi B **45**, 721 (1971).

[19] R. G. Moore, S. Okamoto, H. Li, W. R. Meier, H. Miao, H. N. Lee, M. Hashimoto, D. Lu, E. Dagotto, M. A. McGuire, and B. C. Sales, Phys. Rev. B **106**, 115141 (2022).

[20] W. R. Meier, J. Yan, M. A. McGuire, X. Wang, A. D. Christianson, and B. C. Sales, Phys. Rev. B **100**, 184421 (2019).

[21] B. C. Sales, W. R. Meier, A. F. May, J. Xing, J.-Q. Yan, S. Gao, Y. H. Liu, M. B. Stone, A. D. Christianson, Q. Zhang, and M. A. McGuire, Phys. Rev. Mater. **5**, 044202 (2021).

[22] K. Vijay, L. S. S. Chandra, K. Ali, A. Sagdeo, P. Tiwari, M. K. Chattopadhyay, A. Arya, and S. Banik, Appl. Phys. Lett. **122**, 233103 (2023).

[23] W. R. Meier, M.-H. Du, S. Okamoto, N. Mohanta, A. F. May, M. A. McGuire, C. A. Bridges, G. D. Samolyuk, and B. C. Sales, Phys. Rev. B **102**, 075148 (2020).

[24] S. Ligenza, Phys. Status Solidi B **50**, 379 (1972).

[25] S.-H. Lee, Y. Kim, B. Cho, J. Park, M.-S. Kim, K. Park, H. Jeon, M. Jung, K. Park, J. Lee, and J. Seo, Commun. Phys. **5**, 235 (2022).

[26] B. C. Sales, J. Yan, W. R. Meier, A. D. Christianson, S. Okamoto, and M. A. McGuire, Phys. Rev. Mater. **3**, 114203 (2019).

[27] J. Park, B. Cho, C.-Y. You, and K. Park, J. Alloys Compd. **976**, 173003 (2024).

[28] Z. Lin, C. Wang, P. Wang, S. Yi, L. Li, Q. Zhang, Y. Wang, Z. Wang, H. Huang, Y. Sun, Y. Huang, D. Shen, D. Feng, Z. Sun, J.-H. Cho, C. Zeng, and Z. Zhang, Phys. Rev. B **102**, 155103 (2020).

[29] P. E. Blöchl, O. Jepsen, and O. K. Andersen, Phys. Rev. B **49**, 16223 (1994).

[30] J. P. Perdew, K. Burke, and M. Ernzerhof, Phys. Rev. Lett. **77**, 3865 (1996).

[31] G. Kresse and J. Furthmüller, Phys. Rev. B **54**, 11169 (1996).

[32] A. van de Walle, P. Tiwary, M. de Jong, D. L. Olmsted, M. Asta, A. Dick, D. Shin, Y. Wang, L.-Q. Chen, and Z.-K. Liu, CALPHAD **42**, 13 (2013).

[33] H. J. Monkhorst and J. D. Pack, Phys. Rev. B **13**, 5188 (1976).

[34] V. Petříček, M. Dušek and L. Palatinus, Z. Kristallogr. **229**, 345 (2014).

[35] E. Clementi, D. L. Raimondi, and W. P. Reinhardt, J. Chem. Phys. **47**, 1300 (1967).

[36] D. Multer, J.-X. Yin, Md. S. Hossain, X. Yang, B. C. Sales, H. Miao, W. R. Meier, Y.-X. Jiang, Y. Xie, P. Dai, J. Liu, H. Deng, H. Lei, B. Lian, and M. Z. Hasan, Commun. Mater. **4**, 17 (2023).

[37] X. Chen, Y. Mudryk, A. K. Pathak, W. Feng, and V. K. Pecharsky, J. Magn. Magn. Mater. **436**, 91 (2017).

[38] S. Lin, D. F. Shao, J. C. Lin, L. Zu, X. C. Kan, B. S. Wang, Y. N. Huang, W. H. Song, W. J. Lu, P. Tong, and Y. P. Sun, J. Mater. Chem. C **3**, 5683 (2015).

[39] S. S. Samatham, A. K. Patel, A. V. Lukoyanov, K. G. Suresh, and R. Nirmala, Phys. Chem. Chem. Phys. **23**, 5607 (2021).

[40] Y. Tao, L. Daemen, Y. Cheng, J. C. Neuefeind, and D. Louca, Phys. Rev. B **107**, 174407 (2023).

[41] R. Kumar, A. Chakraborty, S. Fukuoka, F. Damay, E. Kermarrec, P. L. Paulose, and Y. Ihara, Phys. Rev. B **107**, 134432 (2023).

[42] F. Long, K. Mosina, R. Hübner, Z. Sofer, J. Klein, S. Prucnal, M. Helm, F. Dirnberger, and S. Zhou, Appl. Phys. Lett. **123**, 222401 (2023).

[43] I. A. Blech and B. L. Averbach, Phys. Phys. Fiz. **1**, 31 (1964).

[44] M. Kakihana, K. Nishimura, D. Aoki, A. Nakamura, M. Nakashima, Y. Amako, T. Takeuchi, T. Kida, T. Tahara, M. Hagiwara, H. Harima, M. Hedo, T. Nakama, and Y. Ōnuki, J. Phys. Soc. Jpn. **88**, 014705 (2019).

[45] Y. Xie, L. Chen, T. Chen, Q. Wang, Q. Yin, J. R. Stewart, M. B. Stone, L. L. Daemen, E. Feng, H. Cao, H. Lei, Z. Yin, A. H. MacDonald, and P. Dai, Commun. Phys. **4**, 240 (2021).

[46] S.-H. Do, K. Kaneko, R. Kajimoto, K. Kamazawa, M. B. Stone, J. Y. Y. Lin, S. Itoh, T. Masuda, G. D. Samolyuk, E. Dagotto, W. R. Meier, B. C. Sales, H. Miao, and A. D. Christianson, Phys. Rev. B **105**, L180403 (2022).

[47] S. Tougaard, Surf. Sci. **216**, 343 (1989).

[48] S. Doniach and M. Sunjic, J. Phys. C **3**, 285 (1970).

[49] S. Banik, M. K. Chattopadhyay, S. Tripathi, R. Rawat, and S. N. Jha, Sci. Rep. **10**, 12030 (2020).

[50] K. Vijay, D. S. Vavilapalli, A. Arya, S. K. Srivastava, R. Singh, A. Sagdeo, S. N. Jha, K. Kumar, and S. Banik, Sci. Rep. **13**, 8579 (2023).

[51] D. Mondal, S. Banik, C. Kamal, M. Nand, S. N. Jha, D. M. Phase, A. K. Sinha, A. Chakrabarti, A. Banerjee, and T. Ganguli, J. Alloys Compd. **688**, 187 (2016).

[52] F. J. Himpsel, J. Magn. Magn. Mater. **102**, 261 (1991).

[53] J. F. Moulder, W. F. Stickle, P. E. Sobol, and K. D. Bomben, *Handbook of X-Ray Photoelectron Spectroscopy* (Perkin-Elmer, United States of America, 1979).

[54] S. Banik, P. I. Samina, P. N. Rao, H. Srivastava, and A. Sagdeo, Appl. Surf. Sci. **546**, 148896 (2021).

[55] S. Banik, A. Arya, A. Bendounan, M. Maniraj, A. Thamizhavel, I. Vobornik, S. K. Dhar, and S. K. Deb, J. Phys.: Condens. Matter **26**, 335502 (2014).

[56] P. A. Bhobe, A. Chainani, M. Taguchi, T. Takeuchi, R. Eguchi, M. Matsunami, K. Ishizaka, Y. Takata, M. Oura, Y. Senba, H. Ohashi, Y. Nishino, M. Yabashi, K. Tamasaku, T. Ishikawa, K. Takenaka, H. Takagi, and S. Shin, Phys. Rev. Lett. **104**, 236404 (2010).

[57] Z. Liu, M. Li, Q. Wang, G. Wang, C. Wen, K. Jiang, X. Lu, S. Yan, Y. Huang, D. Shen, J.-X. Yin, Z. Wang, Z. Yin, H. Lei, and S. Wang, Nat. Commun. **11**, 4002 (2020).

[58] S. Banik, P. K. Das, A. Bendounan, I. Vobornik, A. Arya, N. Beaulieu, J. Fujii, A. Thamizhavel, P. U. Sastry, A. K. Sinha, D. M. Phase, and S. K. Deb, Sci. Rep. **7**, 4120 (2017).

[59] S. Banik, A. Chakrabarti, D. A. Joshi, A. Thamizhavel, D. M. Phase, S. K. Dhar, and S. K. Deb, Phys. Rev. B **82**, 113107 (2010).

[60] S. Banik, A. Bendounan, A. Thamizhavel, A. Arya, P. Risterucci, F. Sirotti, A. K. Sinha, S. K. Dhar, and S. K. Deb, Phys. Rev. B **86**, 085134 (2012).